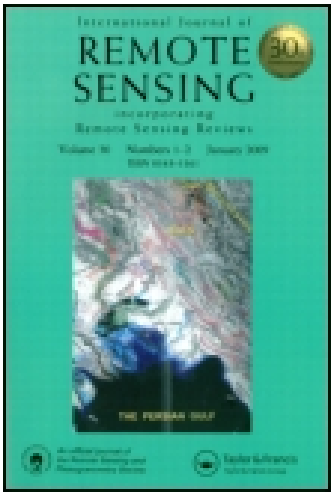

International Journal of Remote Sensing
Publication details, including instructions for authors and subscription information:
http://www.tandfonline.com/loi/tres20

Latent heat flux at the sea surface retrieved from combined TMI and VIRS measurements of TRMM

P. SchlÜssel [a] & A. Albert [a]
[a] Meteorologisches Institut , Ludwig-Maximilians-UniversitÄ
Published online: 25 Nov 2010.

To cite this article: P. SchlÜssel & A. Albert (2001) Latent heat flux at the sea surface retrieved from combined TMI and VIRS measurements of TRMM, International Journal of Remote Sensing, 22:10, 1975-1998

To link to this article: http://dx.doi.org/10.1080/01431160118529

INT. J. REMOTE SENSING, 2001, VOL. 22, NO. 10, 1975–1998

Latent heat flux at the sea surface retrieved from combined TMI and VIRS measurements of TRMM

P. SCHLÜSSEL†‡ and A. ALBERT†§

†Meteorologisches Institut, Ludwig-Maximilians-Universität München
Theresienstraße 37, D-80333 Munich, Germany
‡EUMETSAT, Am Kavalleriesand 31, D-64295 Darmstadt, Germany
§Institut für Methodik der Fernerkundung, DLR, D-82230 Weßling, Germany

(*Received 4 June 1999; in final form 25 January 2000*)

Abstract. Two radiometers of the Tropical Rainfall Measuring Mission (TRMM) were used to retrieve parameters that were necessary to determine the latent heat flux density at the sea surface. The Visible and Infrared Radiometer System (VIRS) was used to measure sea surface temperature. The TRMM Microwave Imager (TMI) measured near-surface wind speed and air-specific humidity. The retrieval schemes for these parameters were derived theoretically by means of radiative transfer simulations and were validated by TRMM data matched with buoy measurements. The validation study revealed deficiencies in the description of the infrared water vapour absorption continuum and in the TMI calibration. Both effects were corrected for so that the desired parameters could be retrieved with adequate accuracy. A global application of the retrieval method to TRMM data for April 1998 is shown.

1. Introduction

The evaporation of the sea surface constitutes a part of the freshwater flux between ocean and atmosphere. The difference between precipitation and evaporation over sea is one of the most important parts of the global hydrological cycle. By the latent heat of evaporation it also accounts for a substantial part of the air–sea energy flux. Direct measurements of the surface evaporation are only possible by means of eddy correlation techniques. These are confined to surface observations and are not possible from satellites. The turbulent water vapour flux at the sea surface is the correlation product

$$E = \rho \overline{w'q'} \tag{1}$$

where w' and q' are the fluctuations of vertical wind velocity and specific humidity above the sea surface, respectively, and ρ is the air density. The fluctuations have to be resolved at a temporal scale of about 10 Hz and averaged over time periods of about 10 minutes to obtain meaningful values of the evaporation (Hasse 1993). Equation (1) is commonly parametrized with the so-called bulk aerodynamic formula, assuming that the evaporation at the surface is driven by the air–sea humidity gradient and that the air–sea exchange increases with wind speed. A recent

International Journal of Remote Sensing
ISSN 0143-1161 print/ISSN 1366-5901 online © 2001 Taylor & Francis Ltd
http://www.tandf.co.uk/journals

formulation of the bulk formula is given by (Fairall *et al.* 1996)

$$E = -C_E(S, \theta_v T_0)\rho S(q_0 - q) \tag{2}$$

where C_E is an exchange coefficient (also known as Dalton number) depending non-linearly on wind speed and stability, θ_v is the virtual potential air temperature, T_0 is the sea surface skin temperature, q_0 is the sea surface specific humidity, q is the air-specific humidity, and

$$S = \sqrt{u^2 + w_g^2} \tag{3}$$

where u is the near-surface wind speed and

$$w_g = \beta(-z_i g u_* T_* / T_a)^{1/3} \tag{4}$$

is the gustiness factor that accounts for evaporation in calm situations, driven by free convection. T_a is the near-surface air temperature, z_i is the atmospheric boundary-layer height, g is the gravitational acceleration, u_* is the friction velocity above the sea surface, $\beta = 1.2$, and

$$T_* = -H/(c_p \rho u_*) \tag{5}$$

is a scaling temperature following the Monin–Obukhov similarity (MOS) where H is the sensible heat flux and c_p is the specific heat of air at constant pressure. The latent heat-flux density is obtained from (2) by multiplying E with the latent heat of evaporation, L, which in turn is a function of the temperature.

The functional dependence of C_E on S and $\theta_v - T_0$ is described by the MOS surface-layer theory (e.g. Panofsky and Dutton 1984). Summarizing the dependencies in (2)–(5) and similar ones for the turbulent flux of momentum leads to mainly three variables that are needed to calculate the evaporation: T_0, u and q. Further knowledge is necessary about the air pressure, p, and temperature as well as the planetary boundary-layer height.

While p and z_i are sufficiently represented by their mean values, the air temperature must be known more precisely. Liu *et al.* (1994) suggest to retrieve the surface air temperature from the air specific humidity (that is retrieved from the satellite measurements) and the assumption of a constant relative humidity of 80% in the marine atmosphere. The usefulness of this coarse parametrization was confirmed by Taurat (1996) for tropical and subtropical situations. The air temperature derived by this method is also entered into the calculation of the sensible heat flux which is needed in (5). The sensible heat flux is calculated with a bulk aerodynamic formula similar to (2).

The use of satellite data to retrieve T_0, u and q for the use with the bulk formula (2) has been elaborated for the sensor combination Advanced Very High Resolution Radiometer (AVHRR) and Special Sensor Microwave/Imager (SSM/I) (Schlüssel *et al.* 1995, Schlüssel 1996). An evaluation of the method has been presented by Schulz *et al.* (1996). The validation studies show that the latent heat flux, derived from instantaneous satellite measurements agree within a standard deviation of 30 W m^{-2} (corresponds to an evaporation of 1 mm day^{-1}) with co-located ship and buoy measurements. Recently, the combined retrieval method has been successfully applied in an air–sea interaction study of the Indian Ocean (Ramesh Kumar and Schlüssel 1998), demonstrating the usefulness of this remote sensing method in climate studies.

The aim of this study is to seek for improvements in the developed remote sensing

methods for tropical and subtropical regions by transferring the techniques for the use with infrared and microwave radiometers carried by the Tropical Rainfall Measuring Mission (TRMM) that is flown as joint US–Japanese satellite mission since November 1997 (Kummerow *et al.* 1998). In the following sections we describe the satellite data as well as the *in situ* measurements employed for radiative transfer calculations and validation studies. Subsequently, the development of the retrieval schemes for T_0, u and q is described. In further sections the validation by means of buoy measurements is shown and the correction of the calibration of the microwave radiometer is discussed. Finally, the derived methods are applied to global TRMM data and fields of the boundary layer parameters as well as the surface latent heat flux are presented.

2. Data

Different datasets are used in this study originating from various sources:

1. TRMM satellite data including measurements from the TRMM microwave Imager (TMI) and the Visible and Infrared Radiometer System (VIRS) for the time period January to June 1998.
2. Atmospheric data entered into the radiative transfer calculations for the theoretical development of the retrieval schemes
3. *In situ* measurements from moored buoys for the validation of the satellite-retrieved boundary-layer parameters.

2.1. *The satellite and its instruments*

TRMM is a satellite dedicated to the observation of tropical precipitation in the latitude band between 38.5°S and 38.5°N. The orbit of TRMM has been chosen to be non sun-synchronous and drifting in order to avoid diurnal signals in long-periodical averages of the retrieved rainfall. The nominal height of the satellite is 333 km; about 16 orbits are completed every day. Besides a precipitation radar and a lightning detector which are not considered in this study TRMM carries two radiometers, TMI and VIRS. Their spectral characteristics are listed in table 1.

TMI and VIRS are used together for the retrieval of the boundary-layer

Table 1. Spectral characteristics of TMI and VIRS.

TMI			VIRS		
Frequency (GHz) polarization	IFOV (km) AT/CT	NEΔT (K)	Wavelength (μm)	IFOV at nadir (km)	NEΔT (K)
10.65 v	63.2/38.2	0.63	0.63	2	—
10.65 h	63.2/38.2	0.64	1.6	2	—
19.35 v	30.4/18.4	0.50	3.75	2	0.07
19.35 h	30.4/18.4	0.47	10.8	2	0.08
21.30 v	27.2/16.5	0.71	12.0	2	0.09
37.00 v	16.0/9.7	0.36			
37.00 h	16.0/9.7	0.31			
85.50 v	7.2/4.4	0.52			
85.50 h	7.2/4.4	0.93			

IFOV, Instantaneous field of view; NEΔT, noise equivalent temperature difference; AT, along-track; CT, cross-track; v, vertical; h, horizontal.

parameters. TMI is a modified SSM/I instrument. Other than SSM/I it has an additional spectral channel at 10.65 GHz and a channel at 21.3 GHz instead of a 22.235 GHz channel. While the 10.65 GHz channel will allow for better wind-speed retrievals in precipitating situations than SSM/I, the 21.3 GHz channel offers better retrievals of the water-vapour column in tropical situations than the 22.235 GHz channel of SSM/I. Owing to the low orbit of TRMM the horizontal resolution of TMI ranges from 4.4 km × 7.2 km (along-track versus cross-track) at 85.5 GHz to 38 km × 63.2 km at 10.65 GHz. TMI scans conically with a local incidence angle near 52.8° (nominal value) resolving 208 samples per scan at 85.5 GHz and 104 samples per scan at the lower frequencies, covering a swath of 758.5 km. Although the TMI is thought to scan conically with a constant viewing angle of 49° (corresponding to a zenith angle of 52.8°) the local incidence angle is not constant due to deviations of the satellite's yaw axis from the local vertical and due to the oblateness of the Earth. Analysis of the true incidence angle which is reported with the data shows a variation of the incidence angle between 46° and 54° in extreme cases. For most measurements, however, the TMI incidence angle varies only within 52.5° and 53.0°. To cover most possible incidence angles all simulations are carried out for 12 different zenith angles selected from normally distributed random numbers with a mean of 52.1° and a standard deviation of 1.1°. The radiometric noise of the measurements varies among the channels and corresponds to temperature differences between 0.3 and 0.9 K.

VIRS is an optical imager similar to AVHRR with spectral channels located in visible, near-infrared and thermal infrared atmospheric windows. The cross-track scan of VIRS covers a swath of 720 km, resolved by 261 pixels in a scan line with a horizontal resolution of 2 km at nadir view. The radiometric noise in the infrared channels is lower than 0.1 K, offering a good opportunity for accurate surface temperature retrievals.

2.2. *Data entering the radiative transfer calculations*

Radiative transfer calculations have to be carried out for a set of atmospheric/oceanic situations representing the global variability over the tropical and subtropical oceans. Such a dataset has been composed from marine radiosonde profiles covering

1. 161 tropical/subtropical radiosondes of the Thermodynamic Initial Guess Retrieval (TIGR) dataset (Chedin *et al.* 1985),
2. 54 aerological datasets from the International Indian Ocean Expedition 1964/65 (Defant 1969),
3. 343 radiosonde ascents collected by the German research vessel *Polarstern* on transit cruises to/from Antarctica during 1986–1989 (Schulz *et al.* 1993).

The 558 datasets contain vertical profiles of temperature and humidity from the surface to the lower stratosphere. They are partly amended by surface temperature and near-surface wind speed. Where this is not the case these variables are generated from random distributions. For the sea surface temperature a mean of $T_a + 1.5$ K has been selected, where T_a is the surface air temperature from the lowest radiosonde level, and a standard deviation of 3 K between air and surface temperature is assumed. The wind speed is taken randomly from a Rayleigh distribution with a mean value of 7.5 m s^{-1}.

Gases other than water vapour are included corresponding their mixing ratios. Some of them like ozone, nitric acid, and chlorofluorocarbons have a non-homogeneous vertical distribution. They are vertically distributed according to

standard profiles described by Anderson *et al.* (1986) and the World Climate Research Program (WCRP 1986). Other gases are assumed to be well mixed (table 2).

Cloud and rain liquid water was not included in the measurements and are randomly scattered into the profiles as well. A mean liquid-water density of $\rho_l = 0.1\,\mathrm{g\,m^{-3}}$ has been inserted with a standard deviation of $0.5\,\mathrm{g\,m^{-3}}$. Resulting values less than 0 are set to 0 and the maximum columnar liquid-water amount of a layer (defined by the vertical resolution of the radiosonde profile) is set to half the corresponding columnar water-vapour content of that layer. The surface rainfall rate is selected randomly from an even distribution between 0 and $5\,\mathrm{mm\,h^{-1}}$. Partly rain or cloud covered areas (due to horizontal inhomogeneity within the sensor's field of view) are generated by combining clear cases with completely cloudy ones and with completely rain-covered situations. The cloud or rain cover is generated from an even random distribution between 0 and 1. The composition is handled as described by Bauer and Schlüssel (1993). This very simplified cloud/rain model seems to be justified here because no attempt is undertaken to retrieve cloud or rain parameters. The inclusion of liquid water is merely thought as to include geophysical noise in the radiative transfer calculations. Additionally, more complete cloud models that are widely employed today for such simulations only represent distinct situations, but not the global variability of cloud and rain water in the tropical atmosphere.

The relative wind direction must be included in the calculation of the surface emissivity. As no information about the wind direction is available from the satellite measurements under consideration and additional information about the actual wind field will not be included in the retrieval schemes the relative wind direction is entered as freely varying parameter. It is chosen from an even random distribution between 0 and 360°.

The extinction of radiation by aerosol particles must be included in the radiative transfer calculations for the infrared channels. This is accomplished by making use of the OPtical Aerosol parameter Catalog (OPAC, Hess *et al.* 1998), defining different realistic aerosol types composed by aerosol particles of various origins. The vertical distribution of the aerosols is implemented by inserting different aerosol layers. Here we have chosen a boundary layer aerosol, extending from the surface to 1.7 km. The aerosol is composed by three components, 'water soluble', 'sea salt in accumulation mode', and 'sea salt in coarse mode' (equally distributed). A second aerosol layer is inserted in the stratosphere between 14 and 26 km, containing only one component,

Table 2. Mixing ratio of absorbing gases included in the radiative transfer calculations.

Gas	Volume mixing ratio
H_2O	variable profile
CO_2	355 ppm
O_3	tropical standard profile
N_2O	0.31 ppm
CO	0.13 ppm
CH_4	1.72 ppm
O_2	20.95%
N_2	78.08%
HNO_3	tropical standard profile
CCl_3F	tropical standard profile
CCl_2F_2	tropical standard profile

a 'dustlike background aerosol'. Mean aerosol particle densities are adopted from Hess *et al.* (1998). The variability of the aerosol is represented by a Gaussian random distribution around the logarithm of these means and standard deviations adopted according to climatological distributions found over oceans (Koepke *et al.* 1997). The optical depths of the resulting combined aerosol layers are 0.22, 0.11 and 0.19 in the 3.7, 10.8 and 12.0 μm channels, respectively. The corresponding range of optical depths covered is 0.01–0.86, 0.01–0.82 and 0.01–1.25, respectively.

2.3. *Validation data*

For the validation of the theoretically elaborated retrieval schemes *in situ* measurements are matched within specified time and space windows with the TRMM measurements. The *in situ* measurements are taken from moored buoys operated by the US National Buoy Data Center in the Atlantic and Pacific Oceans. For the validation of the retrieval methods in this study measurements from 71 buoys have been taken. Their geographical distribution is shown in figure 1. The parameters of interest that are measured by the buoys are surface (bulk) temperature, air temperature, dewpoint temperature, wind vector and air pressure. For the time period January to March 1998 available buoy data are collected and matched with TMI and VIRS data when and where possible. As not all parameters are measured by all buoys, due to requirement to observe different match-up windows for the different parameters, and due to the different cloud/rain constraints in the microwave and infrared measurements the match-ups have been collected as shown in table 3.

Most of the buoys are situated close to coastlines and might therefore produce

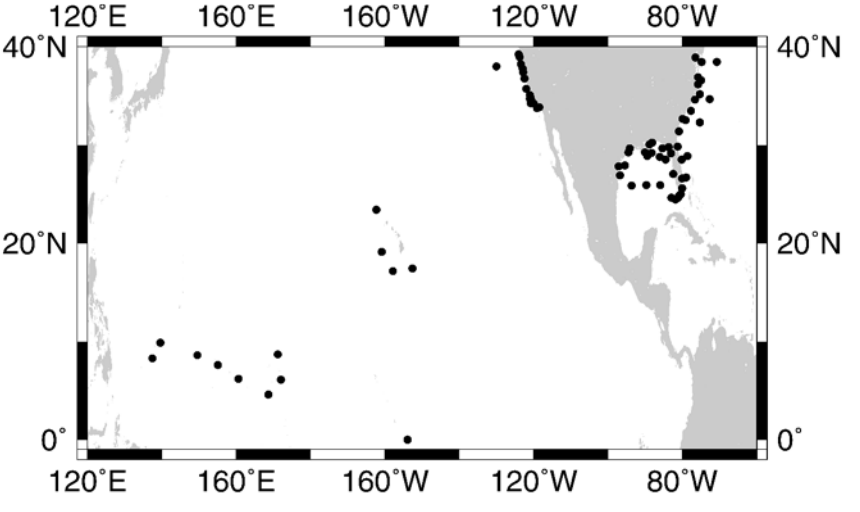

Figure 1. Distribution of moored buoys used for the algorithm validation.

Table 3. Buoy–TRMM match-up database.

Parameter	Time window	Space window	No. of match-ups
Wind speed	30 min	0.3°	36 609
Specific air humidity	30 min	0.3°	12 947
Sea surface temperature	12 h	5 km	3628

unreliable match-ups in cases where the satellite measurements contain partly land-covered areas. To exclude such situations a high-resolution land–ocean database is used to detect land surfaces in the vicinity of the buoys. The land–ocean mask resolves 550 m and should be suited to detect even relatively small coastal irregularities. TMI measurements are excluded from the validation if any land surface is closer in distance than 50 km from the centre of a footprint.

3. Radiative transfer calculations

Radiative transfer calculations are carried out for the set of atmospheric–oceanic situations described in §2.2 for the infrared channels of VIRS and the TMI channels between 10.65 and 37.0 GHz. In both spectral domains the radiative transfer equation is integrated including absorption and emission of surface and atmosphere and surface reflection. Additionally, the space emission is incorporated in the microwave region. The spectral radiance at satellite altitude is represented by

$$L_{v\zeta} = \varepsilon_{v\zeta} B_v(T_0) \exp(-\delta_v^*/\cos\theta) + \int_0^{\delta_n^*} B_v(T(\delta_v)) \exp(-\delta_v/\cos\theta)\, d\delta_v$$
$$+ \rho_{v\zeta} \exp(-\delta_v^*/\cos\theta) \int_{\delta_n^*}^{0} B_v(T(\delta_v)) \exp(-\delta_v/\cos\theta)\, d\delta_v$$
$$+ B_v(T_{sp}) \exp(-2\delta_v^*/\cos\theta) \rho_{v\zeta} \qquad (6)$$

where v is the frequency, ζ is the polarization, B_v is Planck's function, T is the atmospheric temperature, $\varepsilon_{v\zeta}$ is the surface emissivity, $\rho_{v\zeta}$ is the surface reflectivity, δ_v is the optical depth, δ_v^* is the total optical thickness of the atmosphere, θ is the incidence angle, and T_{sp} is the temperature of the galactic space.

The terms on the right side of (6) describe

1. the radiation emitted by the surface at temperature T_0 at an emissivity $\varepsilon_{v\zeta}$ transmitted through the atmosphere with optical depth δ_v^* at an incidence angle of θ to the satellite,
2. the radiation emitted by the atmosphere at temperature T to the satellite,
3. the downward atmospheric emission reflected by the surface with surface reflectivity $\rho_{v\zeta}$ and transmitted to the top of the atmosphere, and
4. the galactic space emission transmitted through the atmosphere, reflected by the surface and transmitted to the satellite.

Vertically and horizontally polarized components of the radiation are calculated for the TMI. For the VIRS only the total radiance is simulated. The numerical model based on (6) has been used for the development of a number of retrieval techniques fitted to the SSM/I and AVHRR radiometers (e.g. Schlüssel and Grassl 1990, Schlüssel and Emery 1990).

3.1. *VIRS simulations*

The band absorption in the 3.7, 10.8 and 12 μm channels of VIRS is described by the k-distribution method (Hollweg 1993) to account for the selective absorption by gases and its band overlapping effects. The k-distributions are determined from line-by-line calculations of the atmospheric transmission in each thermal VIRS channel including as spectral weights the Planck function at different temperatures

and the spectral filter functions of the radiometer. The absorption line parameters are taken from the 1996 edition of the HITRAN database (Rothman *et al.* 1998).

Quasi-continuous absorption by water vapour is included in the calculation of the band absorption. The water vapour continuum in the 3.7 μm channel is described following Bignell (1970). In the 10.8 and 12 μm channels we follow the description by Clough *et al.* (1989) with a modification according to more recent field data of the tropical atmosphere by Kilsby *et al.* (1992). This continuum is described for wavelengths above 10 μm. It is extrapolated here to cover the full range of the 10.8 μm channel which slightly extends to wavelengths below 10 μm. The extrapolation is done using the functional form given by Kilsby *et al.* (1992).

The surface emissivity of the rough sea in the VIRS thermal channels is parametrized in terms of frequency, incidence angle and wind speed according to Masuda *et al.* (1988) with an amendment including a wind-dependent fractional whitecap coverage as described by Monahan and O'Muircheartaigh (1986). The infrared emissivity has been set to $\varepsilon_w = 1$ so that the total emissivity reads

$$\varepsilon(\theta, v, u) = (1 - f(u))\varepsilon_r(\theta, v, u) + f(u)\varepsilon_w \tag{7}$$

where f is the fractional whitecap coverage and ε_r is the emissivity of the rough, but whitecap-free surface. In the VIRS channels the surface reflectivity is approximated by $\rho = (1 - \varepsilon)$. The VIRS is operating in a cross-track scan mode. Consequently, we have chosen to perform all calculations for zenith angles between 0° and 48° in steps of 4°.

3.2. *TMI simulations*

The TMI measurements are considered to be monochromatic as the spectral bandwidth of the radiometer is narrow compared to the spectral signatures of the atmospheric absorption spectrum. The atmospheric absorption included in the radiative transfer model is adopted from Liebe (1989), accounting for gaseous absorption by water vapour and molecular oxygen lines and continua. Additionally, the liquid-water absorption coefficients are given.

A new surface emissivity model for the microwave domain as described by Lemaire (1998) This model is based on first principles physical model of the scattering of electromagnetic waves by the ocean surface. It includes a variety of effects that have not been acknowledged before, describing the surface scattering in great detail. In contrast to the infrared region the parametrization of ρ requires the inclusion of the hemispherically integrated reflection of downwelling radiation, which is accounted for by a model of Guissard *et al.* (1994). Here, a polynomial approximation of the reflectivity, as calculated by Lemaire (1998), is used. The approximation describes the surface reflectivity in terms of friction velocity, of the near-surface atmosphere, surface rain rate, relative wind direction, frequency, polarization, and incidence angle of the radiation.

4. Retrieval algorithms

The retrieval algorithms are derived from the simulated measurements and the datasets inserted into the radiative transfer models assuming that these data represent the correct atmospheric/oceanic situations. To the simulated measurements noise is added representing the radiometric noise with zero mean and a normally distributed random noise with standard deviation corresponding to $NE\Delta T$.

4.1. *Surface wind speed*

Analysis of the simulated data shows that the brightness temperatures measured at 10, 19 and 21 GHz contain sufficient information for a reliable wind-speed retrieval. Additionally, the knowledge about the local incidence angle must be included to account for variations in the surface reflectivity and emissivity with varying viewing angles. Two different tools are used to analyse the simulated data. A multiple linear regression and an artificial neural network. It has been shown by Stogryn *et al.* (1994) that an artificial neural network is an excellent tool for retrieving oceanic wind speed from SSM/I measurements.

A test of both, the linear multiple regression and an artificial neural network, designed a feed-forward fully connected network (Zell 1994) shows that the performance of the latter is superior to the linear approach. In particular, situations with increasing atmospheric liquid-water contents are better handled by the non-linear method without altering the retrieval coefficients.

Several network architectures are tested, involving more or less computational effort; the final choice is made for a network that is not too complicated so that even big data amounts can be processed within realistic time frames (figure 2). Another requirement is the requested retrieval accuracy for the wind speed which has to be better than $1.3\,\mathrm{m\,s^{-1}}$ (standard error). The resulting network consists of a feed-forward network containing one input layer, a hidden, and an output layer with six input units, three hidden units, and one output unit. Each unit is fed with the output of the previous unit o_i by the logistic activation

$$a_j = \frac{1}{1 - \exp\left\{-\left(\sum_i w_{ij} o_i + b_j\right)\right\}} \tag{8}$$

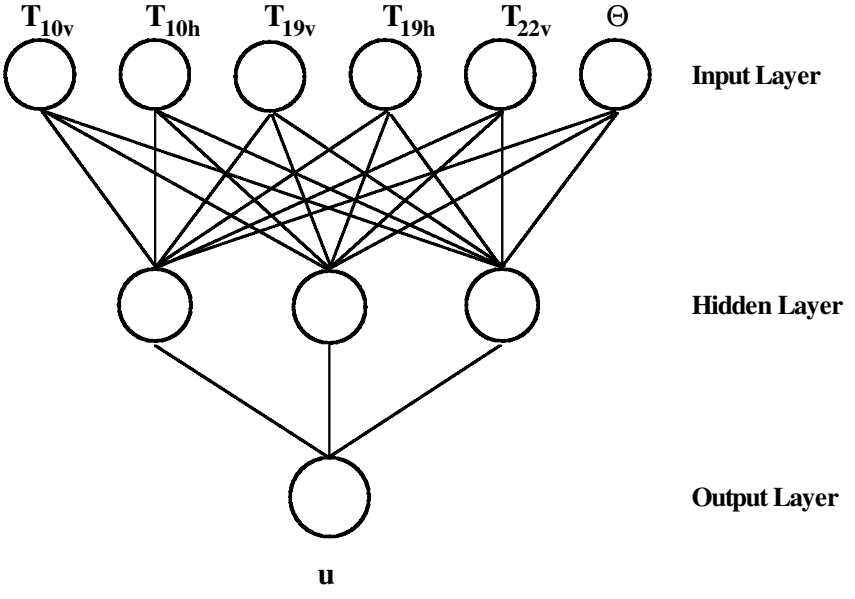

Figure 2. Neural network for wind speed retrieval from TMI.

where b_j are the biases given in table 4 and w_{ij} are the weights given in table 5 and

$$o_j = \begin{cases} 0 & \text{if } a_j < 0 \\ 1 & \text{if } a_j > 1 \\ a_j & \text{otherwise} \end{cases} \tag{9}$$

The coefficients are found by the error-back-propagation method.

The input to the units of the input layer consists of scaled brightness temperatures and scaled incidence angle according to

$$o_i = T_{bi}/A_i, \quad \text{for } i = 1, \ldots, 5 \text{ corresponding to } T_{19v}, T_{19h}, T_{21v}, T_{10v}, T_{10h} \tag{10}$$

and

$$o_6 = \theta/A_6 \tag{11}$$

The network output is the scaled wind speed

$$o_{10} = u/A_{10} \tag{12}$$

The scaling factors A_i, $i = 1, \ldots, 10$ are given in table 4.

Cases with rain rates greater than $5\,\mathrm{mm\,h^{-1}}$ or too high liquid-water columns ($> 120\,\mathrm{mg\,cm^{-2}}$) must be excluded from the wind-speed retrieval as the scattering at liquid-water droplets tends to depolarize the radiation field which cannot be distinguished from the depolarization of the surface reflection caused by increased surface roughness at increasing wind. Furthermore, the atmospheric opacity increases at high liquid-water loadings which diminishes the surface-leaving radiation to an

Table 4. Properties of the artificial neural network retrieving near surface wind speed.

Parameter	Unit	Type	Bias b_j	Scaling A_i
T_{19v}	1	input	0.20707	250 K
T_{19h}	2		−0.68079	210 K
T_{21v}	3		0.29333	270 K
T_{10v}	4		0.10683	220 K
T_{10h}	5		0.36261	170 K
θ	6		−0.77286	57°
	7	hidden	7.21608	
	8		0.30457	
	9		−5.61350	
u	10	output		$35\,\mathrm{m\,s^{-1}}$

Table 5. Weights of the artificial neural network retrieving the near-surface wind speed.

Target j	Source i: Weight w_{ij}		
7	6: 0.93429	5: 5.91802	4: −1.26633
	3: −3.05787	2: 1.91837	1: −8.66964
8	6: −0.91113	5: 0.38558	4: −2.58713
	3: −0.96518	2: 1.81806	1: −2.79569
9	6: 0.77119	5: −14.7098	4: 4.07529
	3: 4.87953	2: −10.7400	1: 13.74966
10	9: −14.6978	8: 3.37857	7: 6.06863

extent that renders the TMI measurements useless in such situations. Therefore, we exclude those TMI measurements where $(T_{37v} - T_{37h}) < 20\,\mathrm{K}$ or $T_{19h} > 190\,\mathrm{K}$. This technique has been proven useful in the wind-speed retrievals from SSM/I already. We do not relax the thresholds in view of the availability of the 10 GHz channels. Rather it is intended to keep high accuracy also in such cases for which the SSM/I allowed only for retrievals with strongly degraded accuracy.

4.2. *Air-specific humidity*

Another analysis of the TMI simulations is performed with respect to the retrieval of near-surface specific humidity. As justified by earlier work (Schulz *et al.* 1993, Schlüssel 1996), the microwave measurements are suited to retrieve the water-vapour column of the 500 m deep atmospheric boundary layer. The boundary layer water-vapour column is highly correlated with the near-surface specific humidity q. Thus, q should be retrievable from TMI measurements. In the earlier studies measurements at 19, 22 and 37 GHz were included. Here, the 22 GHz channel is replaced by one at 21 GHz and additionally, a 10 GHz channel is available. Consequently, a new multivariate analysis is carried out in order to find a useful combination of channels to be included in a retrieval scheme. Again, linear and non-linear analyses are performed. However, in this case the relatively weak non-linearity is superseded by the variance of q not explained by the brightness temperatures so that we chose a linear regression for the retrieval approach. Significance tests show that the 21.8 GHz channel is less suited than the 22.235 GHz channel of SSM/I but still useful to be included. However, the availability of the 10 GHz channel and the restriction to tropical and subtropical situations are favourable and the resulting linear algorithm gives a retrieval accuracy of $1.2\,\mathrm{g\,kg^{-1}}$ for q, which is only slightly worse than that of the corresponding SSM/I algorithm. The choice for the TMI algorithm reads

$$q = a_0 + a_1 T_{10v} + a_2 T_{10h} + a_3 T_{19v} + a_4 T_{19h} + a_5 T_{21v} + a_6 T_{37h} + a_7 \theta \qquad (13)$$

where the a_i, $i = 0, \ldots, 7$ are coefficients optimized by regression (table 6), requiring a significance of 99% to be included. Input to equation (13) are the brightness temperatures in Kelvin and output is q in $\mathrm{g\,kg^{-1}}$.

As for the wind speed cases with high liquid-water columns have to be excluded. The same thresholds are applied to the brightness temperatures as for the wind speed to set the exclusion criterion.

4.3. *Sea surface temperature*

The sea surface temperature T_0 is retrieved from VIRS by employing the well known split- and triple-window algorithms for day- and night-time retrievals, respectively (Schlüssel 1996). Here, we have chosen to include quadratic dependencies on the channel differences in order to account for the strongly non-linear variation of the water-vapour absorption in the tropical atmosphere:

$$T_0 = a_0 + a_1 T_{11} + a_2 (T_{11} - T_{12})(\sec\theta - 1) + a_3 (T_{11} - T_{12})^2 \qquad (14)$$

Table 6. Coefficients for equation (13).

a_0	a_1	a_2	a_3	a_4	a_5	a_6	a_7
−20.44	0.07330	−0.1529	0.3547	0.3339	−0.09973	−0.2432	−0.3795

and

$$T_0 = a_0 + a_1 T_{3,7} + a_2 (T_{3,7} - T_{11}) + a_3 (T_{11} - T_{12}) + a_4 (T_{11} - T_{12})(\sec\theta - 1) \quad (15)$$

have been derived as the best approaches among others with different channel combinations. The initially determined coefficients for 5180 simulated situations are not listed here as the validation study shows that the simulations bear systematic errors which are corrected in the course of the present study. The theoretically derived retrieval accuracy is of the order 0.4 K. However, the real accuracy is rather determined by the ability to detect clouds in the VIRS measurements and to eliminate these cloud contaminated measurements from the temperature retrieval. An inclusion of quadratic terms in (15) did not lead to a significant improvement and have been left out for the sake of simplicity.

5. Validation

The validation studies presented in the following are used to test the theoretically derived retrieval algorithms, to analyse possible discrepancies between *in situ* measurements and satellite retrievals, and to elaborate corrections if necessary.

5.1. *TMI*

The application of the wind algorithm to the TMI data of the match-up dataset and subsequent comparison with the buoy measurements of wind speed shows unexpectedly great systematic differences of about 3 m s^{-1}. The reasons for this deviation could be due to model deficiencies, unrealistic representation of the natural variability in the model simulations or measurement errors. In the course of analysing the different possibilities it has been found that the distributions of brightness temperatures simulated and measured differ systematically for all channels between 10 and 37 GHz. In all cases the measured brightness temperatures are higher than the simulated ones as shown in figure 3 for the 10 GHz channel at horizontal polarization.

Discussion with the TRMM Mission Scientist Dr C. Kummerow at NASA/GSFC on this issue revealed that the TMI suffers from systematic calibration errors. It is thought that the TMI brightness temperatures are correctly calibrated at values near 300 K but show values at space view that are approximately too high by 10 K. To account for this calibration error a correction was suggested that linearly depends on the measured brightness temperature

$$\Delta T_{cor} = (300\,\mathrm{K} - T_b)\frac{\Delta T_{sp}}{300\,\mathrm{K}} \quad (16)$$

where T_b is the brightness temperature measured, and ΔT_{sp} is a temperature offset at space view which has to be determined for each individual channel. This is done by varying the values ΔT_{sp} of all used channels between 10 and 37 GHz until the mean differences between *in situ* and satellite measured wind speed and specific humidity vanish. The resulting values are specified in table 7.

Analysis of three months of data shows that the corrections do not vary with time. Following the calibration of the TMI the wind speed and humidity algorithms are applied again to the satellite measurements co-located with the buoy observations for further comparison. For the wind speed the standard deviation between satellite and buoy-derived values is slightly less than 1.7 m s^{-1}, the wind-speed distributions are similar (figure 4), but not identical. They clearly show that the buoys measure

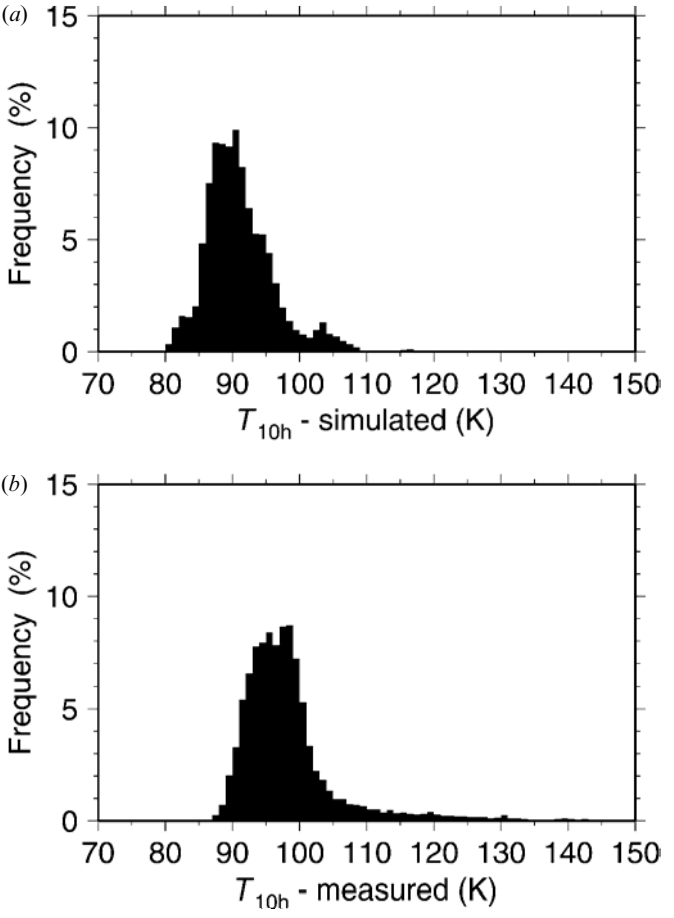

Figure 3. (*a*) Measured and (*b*) simulated distribution of TMI brightness temperatures at 10 GHz, horizontal polarization before correction of the TMI calibration error.

Table 7. Calibration errors ΔT_{sp} at space view for the lower TMI channels.

Channel	10v	10h	19v	19h	21v	37h
ΔT_{sp} (K)	6	6	10	10	10	10

more wind speeds below 1 m s^{-1} which might be due to the fact that the anemometers do not start turning at wind speeds below about 1 m s^{-1} due to adhesive friction. High wind speeds are also less often measured by the buoys as the anemometer height is typically 5 m above the sea level. High wind and swell waves could protect the anemometers from the wind action while the buoys are in wave troughs. The resulting effect is a reduced mean wind speed in a fully developed sea at gale force winds.

For the surface humidity validation we have only 12 947 match-ups as the humidity is only measured by 47 buoys. The comparison (figure 5) between satellite and buoy-measured near-surface specific humidity shows a rather big scatter. The

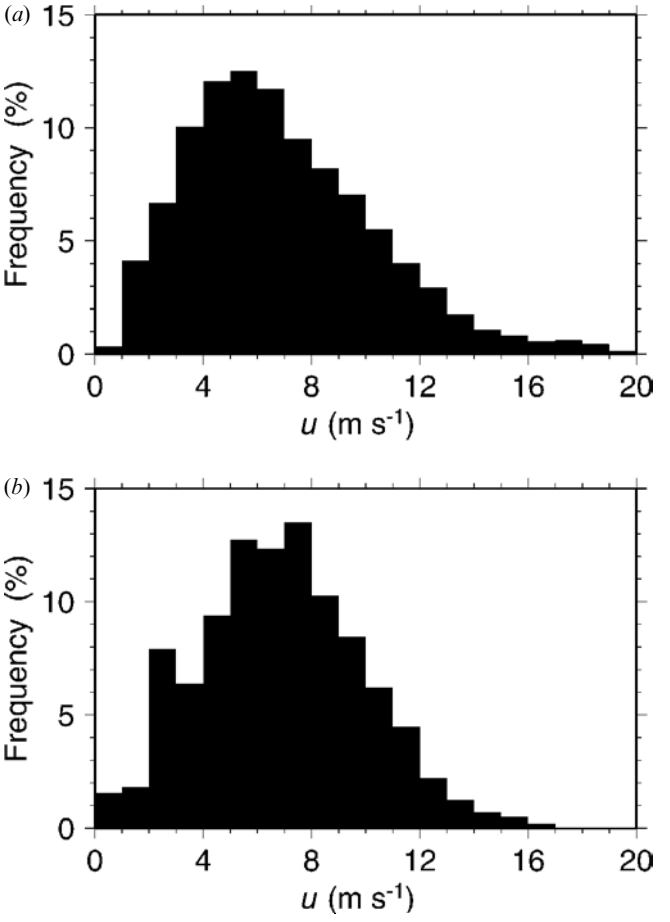

Figure 4. Wind speed distributions at the buoy locations for the time period January to March 1998 as derived from TMI (*a*) and buoy measurements (*b*).

standard deviation between both is 1.9 g kg^{-1}. This is slightly worse compared to the validation results obtained for the humidity retrieval with SSM/I in the tropical and subtropical latitudes (40° S–40° N) where a standard deviation of 1.8 g kg^{-1} was found between satellite and *in situ* measurements (Schlüssel *et al.* 1995).

5.2. *VIRS*

Before any comparisons can be performed between buoy and satellite-derived sea surface temperature the VIRS measurements have to undergo a thorough check for cloud contamination. Earlier studies have shown that all available spectral channels should be included for a proper cloud detection (e.g. Olesen and Grassl 1985, Saunders and Kriebel 1988).

The cloud detection scheme employed here begins with an application of a high-resolution land mask to eliminate measurements which are too close to the coastlines. A distance of 5 km has been chosen as minimum distance between VIRS measurement and any coastline. Next, the spatial coherence is tested in a 3×3 pixel field (Thiermann and Ruprecht 1992). The 11 μm brightness temperature of the pixel

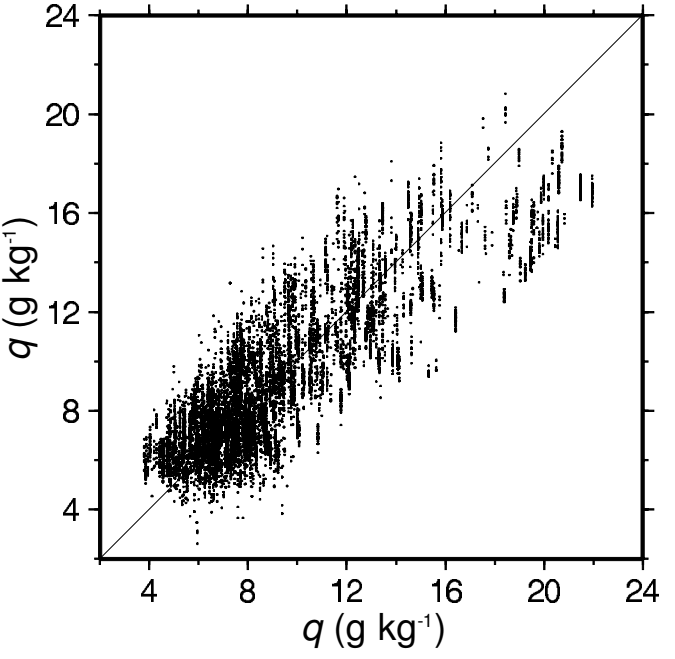

Figure 5. Comparison between satellite-derived near-surface air-specific humidity q_S (ordinate) and buoy-measured humidity q_B (abscissa).

must not deviate by more than 1 K from the mean of the nine adjacent measurements. Subsequently, the 3.7 and 11 μm brightness temperatures are checked. They have to be greater than

$$T_{th} = T_{eq} \cos\left(\varphi \times \arccos\left(\frac{T_{40}}{T_{eq}}\right) \Big/ 40\right) \tag{17}$$

where $T_{eq} = 17°\mathrm{C}$ and $T_{40} = 9°\mathrm{C}$, allowing for minimum brightness temperatures of 17°C at the equator and 9°C at 40° latitude, respectively. The brightness-temperature difference $T_{11} - T_{12}$ must lie in the range $0 \leqslant T_{11} - T_{12} \leqslant 3.5\,\mathrm{K}$. During night, the difference $T_{3.7} - T_{11}$ is tested, it must be within $0 \leqslant T_{3.7} - T_{11} \leqslant 3\,\mathrm{K}$. During daytime, the solar channels are used. Their flux densities must be in the range $0 \leqslant L_1 \leqslant 5\,\mathrm{mW\,cm^{-2}\,\mu m^{-1}}$ and $0 \leqslant L_2 \leqslant 1\,\mathrm{mW\,cm^{-2}\,\mu m^{-1}}$ and their ratio is required to be within $0.05 \leqslant L_2/L_1 \leqslant 0.2$ to identify the measurement as cloud-free. Under twilight conditions (solar zenith angle $>90°$ but L_1 and L_2 still greater than zero) the thresholds are modified so that $0 \leqslant L_1 \leqslant 2\,\mathrm{mW\,cm^{-2}\,\mu m^{-1}}$ and $0 \leqslant L_2 \leqslant 0.5\,\mathrm{mW\,cm^{-2}\,\mu m^{-1}}$, and $0.1 \leqslant L_2/L_1 \leqslant 5$ must be fulfilled.

Threshold values for these cloud tests have been obtained iteratively by visual inspection of the VIRS images. They are rigorous in the sense that doubtful cases are rather excluded than retained as cloud-free. The tests are henceforth used also in the operational processing of the VIRS data.

The comparison of sea surface temperatures retrieved from VIRS with those measured by the buoys have to be performed with great care because the satellite-derived surface temperature represents an average temperature of the upper few

micrometres of the ocean while the buoys measure the temperature in the upper part of the mixed layer at a depth of about one metre. The difference between both temperature measurements is always determined by the temperature difference across the oceanic cool skin and, temporarily, by the temperature difference across the diurnal thermocline (Schlüssel *et al.* 1990). Consequently, we must expect a systematic difference between buoy and satellite measured temperature of few tenths of a Kelvin. This systematic difference is confirmed by the comparison. During night-time the mean difference between buoy and satellite measurements is 0.36 K, during daytime it is 0.14 K, which both fit well to the known diurnal variability of the bulk versus skin temperature difference.

At the same time, other systematic differences appear in the comparison. They consist of a positive correlation of the difference ΔT between buoy and satellite measurements with the buoy measurements. This means that the atmospheric correction applied to the satellite measured brightness temperature increases with increasing surface temperature and therefore with increasing atmospheric water-vapour column. The most likely source for this discrepancy lies in an inaccurate description of the water-vapour continuum absorption. It has already been pointed out by Rudman *et al.* (1994) that the magnitude of the continuum absorption still is underestimated by the model of Kilsby *et al.* (1992) although it has undergone substantial changes with respect to earlier descriptions. A further modification of the continuum absorption seems to be necessary at wavenumbers $920\,\mathrm{cm}^{-1} \leqslant \kappa \leqslant 1050\,\mathrm{cm}^{-1}$ which affects the 10.8 μm channel only. A 25% increase of the continuum absorption coefficient k_{κ} above $1000\,\mathrm{cm}^{-1}$, no change at $920\,\mathrm{cm}^{-1}$ and a linear interpolation of this correction between 920 and $1000\,\mathrm{cm}^{-1}$ leads to the best results in minimizing the correlation between ΔT and buoy-measured surface temperature.

The continuum absorption coefficients finally adopted are shown in figure 6 together with those of Kilsby *et al.* (1992) for two water-vapour densities of $\rho_w = 1\,\mathrm{g\,m}^{-3}$ and $\rho_w = 10\,\mathrm{g\,m}^{-3}$. The resulting coefficients for retrieval models (14) and (15) obtained after final modification of the continuum absorption are listed in table 8.

Buoy and satellite measured surface temperature are compared in figure 7 separately for day and night conditions. As expected, we find a mean difference between buoy and satellite measured temperature of 0.14 K and 0.36 K during day and night, respectively. The standard deviation is 0.68 K in both cases. The systematic deviations are in line with our picture of the oceanic cool skin which is most pronounced in cloud-free areas during night-time. Cloud-free situation is also the required condition for infrared remote sensing of sea surface temperature. During daytime the absorption of solar radiation in the upper ocean partly compensates for the cool skin effect in calm situations, thus leading to a smaller systematic difference (Soloviev and Schlüssel 1996).

6. Application

The retrieval schemes elaborated are applied to a time series of TMI and VIRS data to obtain monthly mean fields of surface temperature, wind speed, air humidity and latent heat flux. The VIRS and TMI data are combined by binning both to a $0.25^\circ \times 0.25^\circ$ grid, where the TMI data are assigned to the nearest grid bin and the VIRS data are averaged over the corresponding bins. We have chosen to present the month of April 1998. In view of the non-linearity involved in equations (1) to (5) it is not opportune to first calculate monthly mean values of T_0, u, q and then to use

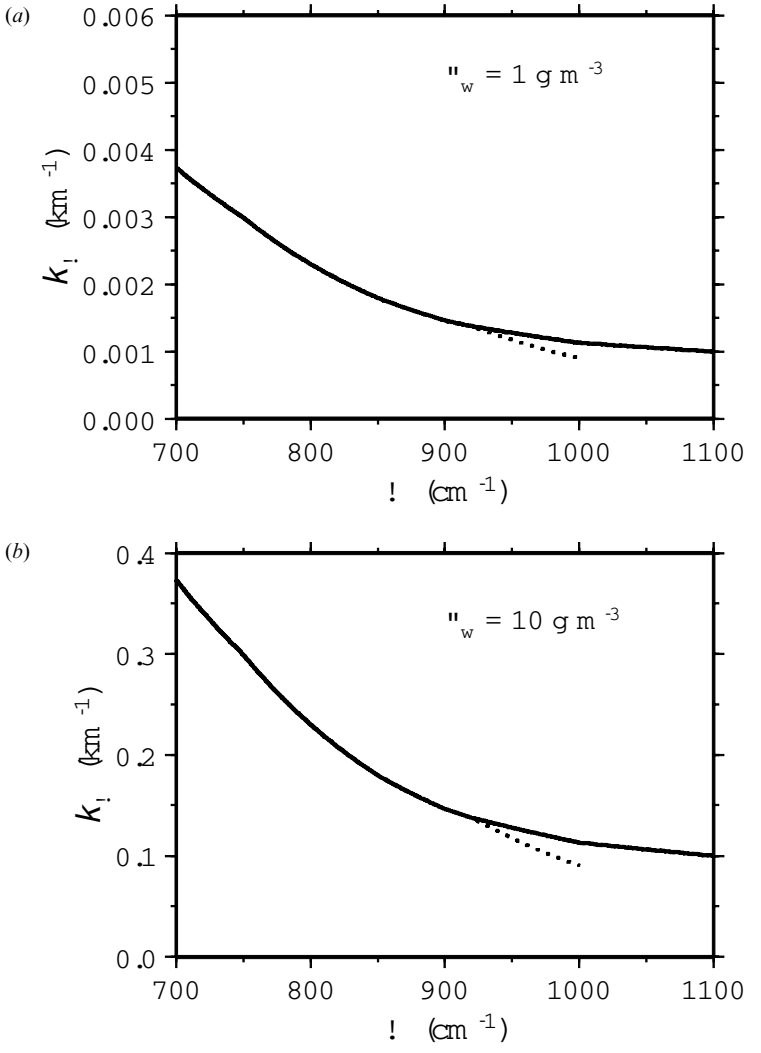

Figure 6. Absorption coefficient of the water-vapour continuum for absolute humidities of 1 g m^{-3} (*a*) and 10 g m^{-3} (*b*); the dotted lines represent the values calculated according to Kilsby *et al.* (1992), the solid lines include the correction above 920 cm^{-1}.

Table 8. Coefficients for retrieval models (14) and (15).

Model	a_0	a_1	a_2	a_3	a_4
Day (14)	−5.16	1.02145	−0.9373	0.02148	0.6674
Night (15)	−4.60	1.01557	−0.7469	1.9701	−0.6235

these averages for the computation of *E*. Rather it is indicated to derive the latent heat flux from individual TMI and VIRS measurements. This is done in the following where possible. However, the measurement of sea surface temperature requires cloud-free atmospheric situations, so that in cloudy areas only wind speed and humidity are measured. In such cases no latent heat-flux retrievals were possible if the surface

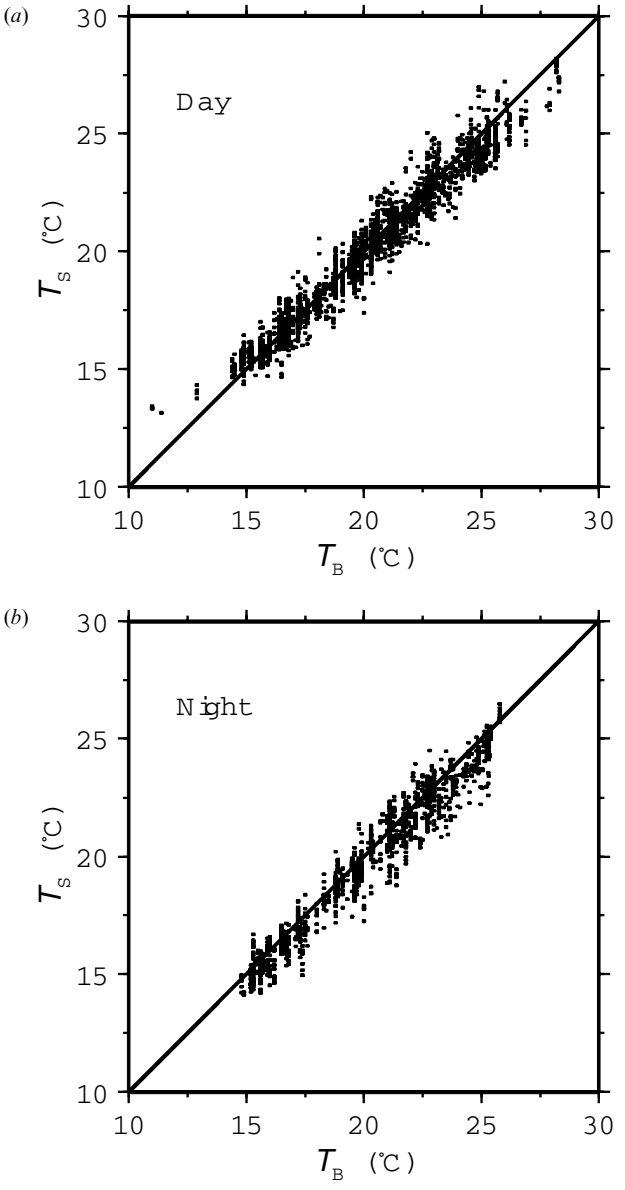

Figure 7. Comparison between satellite-derived sea surface temperature T_s and buoy-measured temperature T_B, (*a*) day, (*b*) night.

temperature would not be a rather stable parameter. Owing to the large heat capacity of sea water and the fact that the upper ocean is well mixed only small temporal changes in the surface temperature are expected. The situation is different in clear areas where strong insolation during daytime and excessive nocturnal cooling of the surface can cause diurnal changes. Fortunately, in such situations the infrared measurements of T_0 are more frequent. Hence, the error introduced in E by assuming that the surface temperature stays constant over a certain time period, say 1 or 2 weeks, remains small. Even over a month we do not find greater variations in the

surface temperature where persistent cloud cover only allows few measurements in a month as is the case in the inter tropical convergence zone. But, there are areas in the tropical ocean where no surface temperature measurement was possible as all during April 1998 (figure 8). The area around Indonesia is known for persistent cloud cover and a wide region was not covered by temperature measurements after 20 days. The eastern equatorial Pacific, however, suffered from excessive cloud coverage during this month because of the 1997/98 El Niño event.

The monthly fields of u and q completely cover the oceans (figure 9) as only few

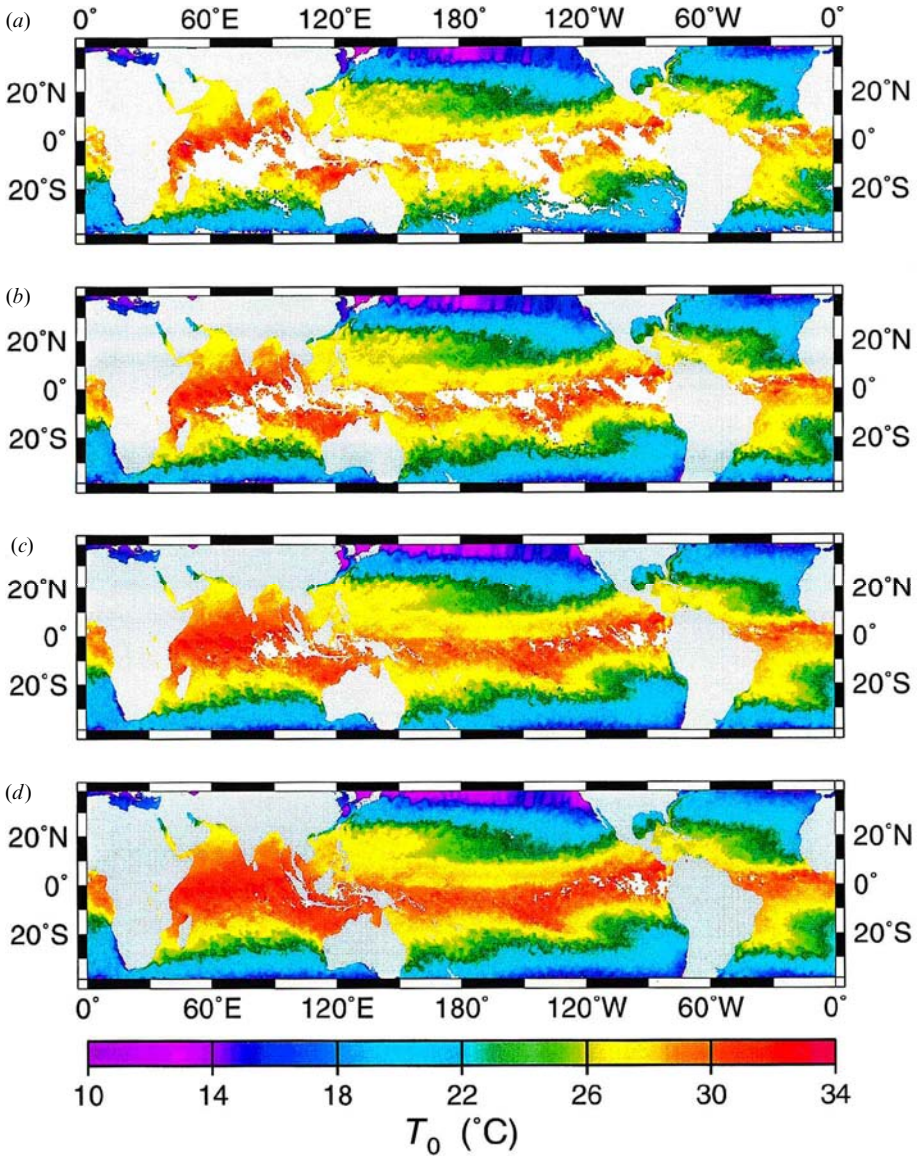

Figure 8. Mean fields of sea surface temperature as measured by VIRS in April 1998. (*a*) First five days, (*b*) first 10 days, (*c*) first 20 days and (*d*) entire month. White areas indicate regions without measurements during the specified time period.

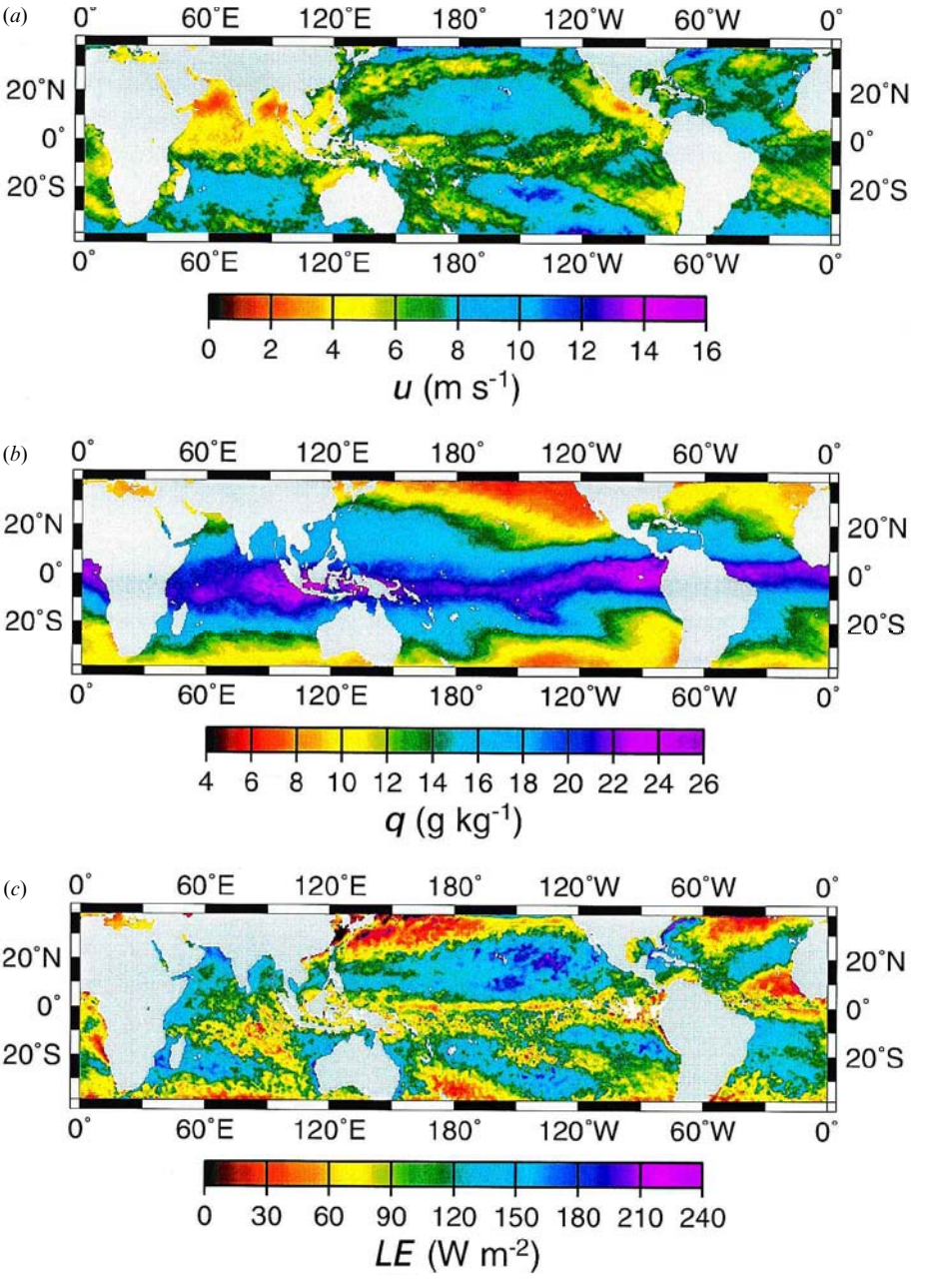

Figure 9. Mean fields of near-surface wind speed (*a*) and near-surface air humidity (*b*) as measured by TMI in April 1998, and mean field of ocean to atmosphere latent heat flux calculated from VIRS-derived surface temperature and TMI retrieved wind and humidity (*c*). White areas indicate regions with missing information.

measurements have to be rejected because of opaque clouds or rain in the sensor's field of view. Additionally, all areas close to coastlines are excluded to keep a minimum distance of 50 km between the centre of a footprint and the nearest coastlines.

The latent heat flux calculated from T_0, u and q as retrieved from VIRS and TMI for April 1998 covers a wide range of values. Nearly vanishing fluxes are found in the northern China Sea and the North Pacific Ocean, where warm and moist air is advected over relatively cold water. Maximum values exceeding 200 W m^{-2} are seen in the subtropical region of the NE and SE Pacific Ocean where the sea–air humidity differences are big and the wind speed is greater than on average.

7. Conclusion

TRMM measurements are used to calculate the latent heat flux at the sea surface. Retrieval models for the measurement of sea surface temperature, surface wind speed and near-surface air humidity are elaborated by means of radiative transfer calculations and validated with buoy measurements. The theoretical study has shown that the single parameters needed for the calculation of the surface latent heat flux can be retrieved from the VIRS and TMI radiometers:

- The sea surface temperature can be obtained with an accuracy near 0.4 K from measurements at 3.7, 11 and 12 μm. A quadratic split-window approach has been selected for daytime and a linear triple-channel algorithm for night-time.
- The near-surface wind speed is retrieved with a predicted accuracy of 1.3 m s^{-1} from a simple artificial neural network using measurements at 10, 19 and 21 GHz.
- The near-surface air humidity can be measured with the TMI channels at 10, 19, 21 and 37 GHz, the predicted accuracy is 1.2 g kg^{-1}.

The validation studies carried out with TRMM measurements co-located to buoy observations in the time period January to March 1998 led to the following results:

- The water-vapour continuum absorption was not properly described by the available models. This fact caused a correlation between buoy versus satellite measured temperature differences and the buoy-measured surface temperature. This effect could be removed by a modified description of the continuum absorption coefficient. The modification consists in a spectrally varying increase of the coefficients with a maximum correction of 25% near 10 μm.
- After correction of the continuum absorption and re-iterated radiative transfer simulations, leading to new retrieval coefficients, a standard deviation of 0.7 K is found between satellite and buoy measurements, excluding the effect of the temperature difference between skin measured by the satellite and buoy-measured bulk temperature. This latter systematic difference amounts –0.36 K during night and -0.14 K during daytime.
- The distribution of simulated and measured TMI measurements show systematic differences because of TMI calibration errors. A frequency-dependent correction is proposed that leads to useful satellite measurements which can be entered into the developed retrieval schemes to obtain bias-free wind-speed and humidity measurements. The standard deviations between satellite-derived and *in situ* measurements of wind speed and air specific humidity are 1.7 m s^{-1} and 1.9 g kg^{-1}, respectively.
- Threshold values for given cloud detection methods are proposed. The methods adopted use all VIRS channels in a globally valid scheme to detect clouds before using the VIRS measurements to calculate sea surface temperature.

The application of the developed methods to one month of global data (April 1998)

shows that the infrared measurements are sufficiently dense to obtain almost complete coverage of tropical and subtropical (within the scope of TRMM) oceans with sea surface temperature measurements. Compared with earlier retrievals of the latent heat, based on AVHRR and SSM/I measurements (Schlüssel 1996), improvements could be found for the surface temperature and wind-speed retrievals in tropical regions. The retrieval of the near-surface air humidity is slightly degraded when compared with the SSM/I-based method.

Acknowledgements

This study was funded by the European Space Agency in the frame of the EuroTRMM project. The TRMM data were kindly delivered by the TRMM Science and Data Information System. Both supports are gratefully acknowledged. We are indebted to Chris Kummerow for valuable hints in handling the TRMM data and to David Lemaire for supplying the computer code calculating the rough sea emissivity. Thanks are due to Darrel Knoll at the National Data Buoy Center who made available the buoy data. All figures have been drafted with free software supplied by Wessel and Smith (1991).

References

Anderson, G. P., Clough, S. A., Kneizys, F. X., Chetwynd, J. H. and Shettle, E. P., 1986, AFGL atmospheric constituents profiles (0–120 km). Report AFGL-TR-86-0110, Air Force Geophysics Laboratory, Hanscom, MA, U.S.A.

Bauer, P., and Schlüssel, P., 1993, Rainfall, total water, ice water and water vapour over sea from polarized microwave simulations and SSM/I data. *Journal of Geophysical Research*, **98**, 20737–20760.

Bignell, K. J., 1970, The water-vapour infrared continuum. *Quarterly Journal of the Royal Meteorological Society*, **96**, 390–403.

Chedin, A., Scott, N. A., Wahiche, C., and Moulinier, P., 1985, The improved initialization inversion method: a high-resolution physical method for temperature retrievals from satellites of the TIROS-N series. *Journal of Climate and Applied Meteorology*, **24**, 128–143.

Clough, S. A., Kneizys, F. X., and Davies, E. W., 1989, Line shape and the water vapor continuum. *Journal of Atmospheric Research*, **23**, 229–241.

Defant, F., 1969, Aerologische Daten gewonnen durch Radiosonden-Aufstiege während der Indischen Ozean Expedition, 1964/, 1965 des Forschungsschiffes 'Meteor'. *'Meteor' Forschungsergebnisse, Reihe B*, **4**, Meteorologie und Aeronomie.

Fairall, C., Bradley, E. F. Rodgers, D. P. Edson, J. B. and Young, G. S. 1996, The TOGA COARE bulk flux algorithm. *Journal of Geophysical Research*, **101**, 3747–3764.

Guissard, A., Sobieski, P., and Laloux, A., 1994, Radiative transfer equation with surface scattering for ocean and atmospheric parameters retrieval from radiometric measurements. *International Journal of Remote Sensing*, **15**, 1743–1760.

Hasse, L., 1993, Observations of air sea fluxes. In *Energy and Water Cycles in the Climate System*, NATO ASI Series, edited by E. Raschke and D. Jakob (Berlin: Springer Verlag), pp. 263–293.

Hess, M., Koepke, P., and Schult, I., 1998, Optical properties of aerosols and clouds: the software package OPAC. *Bulletin of the American Meteorological Society*, **79**, 831–844.

Hollweg, H.-D., 1993, A k-distribution method considering centers and wings of atmospheric absorption lines. *Journal of Geophysical Research*, **98**, 2747–2756.

Kilsby, C. G., Edwards, D. P., Saunders, R. W., and Foot, J. S. 1992, Water-vapour continuum absorption in the tropics: aircraft measurements and model comparisons. *Quarterly Journal of the Royal Meteorological Society*, **118**, 715–748.

Koepke, P., Hess, M., Schult, I., and Shettle, E. P., 1997, Global aerosol data set. Report 243, Max-Planck-Institut für Meteorologie, Hamburg.

Kummerow, C., Barnes, W., Kozu, T., Shiue, J., and Simpson, J. 1998, The Tropical Rainfall

Measuring Mission (TRMM) sensor package. *Journal of Atmospheric and Oceanic Technology*, **15**, 809–817.

LEMAIRE, D., 1998, Non-fully developed sea state characteristics from real aperture radar remote sensing. PhD dissertation, Université Catholique de Louvain, Louvain, 220 pp.

LIEBE, H. J., 1989, MPM—An atmospheric millimeter wave propagation model. *International Journal of Infrared and Millimeter Waves*, **10**, 631–649.

LIU, W. T., ZHANG, A., and BISHOP, K. B. 1994, Evaporation and solar irradiance as regulators of sea surface temperature in annual and interannual changes. *Journal of Geophysical Research*, **99**, 12623–12637.

MASUDA, K., TAKASHIMA, T., and TAKAYAMA, Y., 1988, Emissivity of pure and sea waters for the model sea surface in the infrared window regions. *Remote Sensing of Environment*, **24**, 313–329.

MONAHAN, E. C., and O'MUIRCHEARTAIGH, I. G., 1986, Whitecaps and the passive remote sensing of the ocean surface. *International Journal of Remote Sensing*, **7**, 627–642.

OLESEN, F. S., and GRASSL, H., 1985, Cloud detection and classification over oceans at night with NOAA-7. *International Journal of Remote Sensing*, **6**, 1435–1444.

PANOFSKY, H. A., and DUTTON, J. A., 1984, *Atmospheric Turbulence Models and Methods for Engineering Application* (New York: Wiley), 397 pp.

RAMESH KUMAR, M. R., and SCHLÜSSEL, P., 1998, Air–sea interaction over the Indian Ocean during the two contrasting monsoon years, 1987 and 1988, studied with satellite data. *Theoretical and Applied Climatology*, **60**, 19–231.

ROTHMAN, L. S., RINSLAND, C. P., GOLDMAN, A., MASSIE, S. T., EDWARDS, D. P., FLAUD, J.-M, PERRIN, A. CAMY-PEYRET, C., DANA, V., MANDIN, J.-Y., SCHROEDER, J., MCCANN, A., GAMACHE, R. R., WATTSON, R. B., YOSHINO, K., CHANCE, K. V., JUCKS, K. W., BROWN, L. R., NEMCHINOV, V., and VARASANI, P., 1998, The HITRAN molecular spectroscopic database and HAWKS (HITRAN atmospheric workstation), 1996 edition. *Journal of Quantitative Spectroscopy and Radiative Transfer*, **60**, 665–710.

RUDMAN, S. D., SAUNDERS, R. W., KILSBY, C. G., and MINNETT, P. J., 1994, Water vapour continuum absorption in mid-latitudes: aircraft measurements and model comparisons. *Quarterly Journal of the Royal Meteorological Society*, **120**, 795–807.

SAUNDERS, R. W., and KRIEBEL, K. T., 1988, An improved method for detecting clear sky and cloudy sky radiances from AVHRR data. *International Journal of Remote Sensing*, **9**, 123–150.

SCHLÜSSEL, P., 1996, Satellite remote sensing of evaporation over sea. In *Radiation and Water in the Climate System: Remote Measurements*, edited by E. Raschke, NATO ASI Series, I45 (Berlin: Springer Verlag), pp. 431–461.

SCHLÜSSEL, P., and EMERY, W. J., 1990, Atmospheric water vapour over oceans from SSM/I measurements. *International Journal of Remote Sensing*, **11**, 753–760.

SCHLÜSSEL, P., and GRASSL, H., 1990, SST in polynias: a case study. *International Journal of Remote Sensing*, **11**, 933–945.

SCHLÜSSEL, P., EMERY, W. J., GRASSL, H., and MAMMEN, T., 1990, On the bulk-skin temperature difference and its impact on satellite remote sensing of sea surface temperature. *Journal of Geophysical Research*, **95**, 13341–13356.

SCHLÜSSEL, P., SCHANZ, L., and ENGLISCH, G., 1995, Retrieval of latent heat flux and longwave irradiance at the sea surface from SSM/I and AVHRR measurements. *Advances in Space Research*, **16**, 106–116.

SCHULZ, J., SCHLÜSSEL, P., and GRASSL, H. 1993, Water vapour in the atmospheric boundary layer over oceans from SSM/I measurements. *International Journal of Remote Sensing*, **14**, 2773–2789.

SCHULZ, J., MEYWERK, J., EWALD, S., and SCHLÜSSEL, P., 1996, Evaluation of satellite-derived latent heat fluxes. *Journal of Climate*, **10**, 2782–2795.

SOLOVIEV, A. V., and SCHLÜSSEL, P., 1996, Evolution of cool skin and direct air–sea gas transfer coefficient during daytime. *Boundary-Layer Meteorology*, **77**, 45–68.

STOGRYN, A. P., BUTLER, C. T., and BARTOLAC, T. J., 1994, Ocean surface wind retrievals from special sensor microwave imager data with neural networks. *Journal of Geophysical Research*, **99**, 981–984.

TAURAT, D., 1996, Windfelder über See unter Verwendung von Satellitendaten und Druckanalysen. Berichte aus dem Zentrum für Meeres- und Klimaforschung der Universität Hamburg, Hamburg, **A22**, 1–101.

THIERMANN, V., and RUPRECHT, E., 1992, A method for the detection of clouds using AVHRR infrared observations. *International Journal of Remote Sensing*, **10**, 1829–1841.

WESSEL, P., and SMITH, W. H. F., 1991, Free software helps map and display data. *Transactions of the American Geophysical Union*, **72**, 441 and 445–446.

WORLD CLIMATE RESEARCH PROGRAMME, 1986, A primary cloudless standard atmosphere for radiation computation, WCP-112, WMO/TD-No 24. World Meteorological Organization, Geneva, 36 pp.

ZELL, A., 1994, *Simulation Neuronaler Netze* (Munich: R. Oldenbourg Verlag), 624 pp.